Chemical Science

ROYAL SOCIETY OF CHEMISTRY

EDGE ARTICLE

View Article Online
View Journal | View Issue

Check for updates

Cite this: *Chem. Sci.*, 2020, **11**, 3978

All publication charges for this article have been paid for by the Royal Society of Chemistry

Received 23rd December 2019
Accepted 19th March 2020

DOI: 10.1039/c9sc06500h

rsc.li/chemical-science

Twist and sliding dynamics between interpenetrated frames in Ti-MOF revealing high proton conductivity†

Jing Cao,[a] Wenjie Ma,[b] Kangjie Lyu,[b] Lin Zhuang,[ab] Hengjiang Cong*[b] and Hexiang Deng*[ab]

We report the design and synthesis of a titanium catecholate framework, MOF-217, comprised of 2,4,6-tri(3,4-dihydroxyphenyl)-1,3,5-triazine (TDHT) and isolated TiO_6 clusters, with 2-fold interpenetrated **srs** topology. The dynamics of the organic linker, breaking the C_{3h} symmetry, allowed for reversible twist and sliding between interpenetrated frames upon temperature change and the inclusion of small molecules. Introduction of 28 wt% imidazole into the pores of MOF-217, 28% Im-in-MOF-217, resulted in four orders of magnitude increase in proton conductivity, due to the appropriate accommodation of imidazole molecules and their proton transfer facilitated by the H-bond to the MOF structure across the pores. This MOF-based proton conductor can be operated at 100 °C with a proton conductivity of 1.1×10^{-3} S cm^{-1}, standing among the best performing anhydrous MOF proton conductors at elevated temperature. The interframe dynamics represents a unique feature of MOFs that can be accessed in the future design of proton conductors.

Introduction

Structure dynamics is one of the key features in biological systems that allows for accommodation of guest molecules, selective chemical conversions, and concerted ion transportation.[1–3] Introduction of such controllable dynamics into artificial solid-state materials is challenging, but it is likely to promise enhanced physical and chemical properties.[4–10] Metal–organic frameworks (MOFs), constructed using linking organic molecules with metal joints, provide precise control on their pore size and geometry;[11–13] thus they have great potential to exercise structure dynamics and to optimize their properties (Scheme 1 and S1†), such as proton conductivity.[14–17] One ideal way to introduce dynamic operations into MOFs is stitching molecular building blocks with mechanically interlocked components into the framework (Scheme S1B†).[18] Such building blocks usually occupy a relatively large space; thus, this approach is demanding on the pore size of the corresponding MOF. Another way to create structure dynamics in MOFs is interpenetration, where two or more sets of identical frames coexist in the same crystal but remain geometrically catenated.[19,20] The shift between these sets gives rise to structure dynamics and leads to the opening and closing of the pores, hence precisely controlling the behaviour of guest molecules (Scheme S1C†).[21] Dynamics in neither approach involves the change of coordination geometry at the metal joints, which is different from the common flexible MOFs (Scheme S1A†).[22,23] The number of MOFs exhibiting interpenetrated structures is large, but most of them are dense and not suited for structure dynamics or interaction with guest molecules. For the rest of them, only a few allow for shift between different sets of frames, but for the ones that do have such capability, they usually exhibit excellent properties, such as selective inclusion and gas separation.[21,24]

In this study, we revealed that dynamics between frames in an interpenetrated MOF offers excellent accommodation for molecules to achieve high proton conductivity under anhydrous conditions at elevated temperature. Specifically, we synthesized

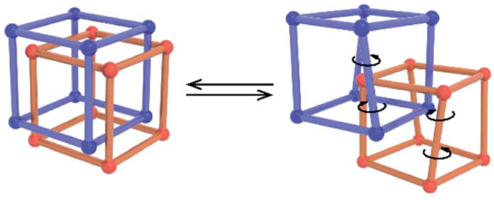

Scheme 1 Twist and sliding dynamics in MOFs with an interpenetrated structure.

---

[a] UC Berkeley-Wuhan University Joint Innovative Center, The Institute for Advanced Studies, Wuhan University, Luojiashan, Wuhan 430072, China. E-mail: hdeng@whu.edu.cn

[b] College of Chemistry and Molecular Sciences, Wuhan University, Luojiashan, Wuhan 430072, China

† Electronic supplementary information (ESI) available. CCDC 1964929–1964931, 1993021. For ESI and crystallographic data in CIF or other electronic format see DOI: 10.1039/c9sc06500h

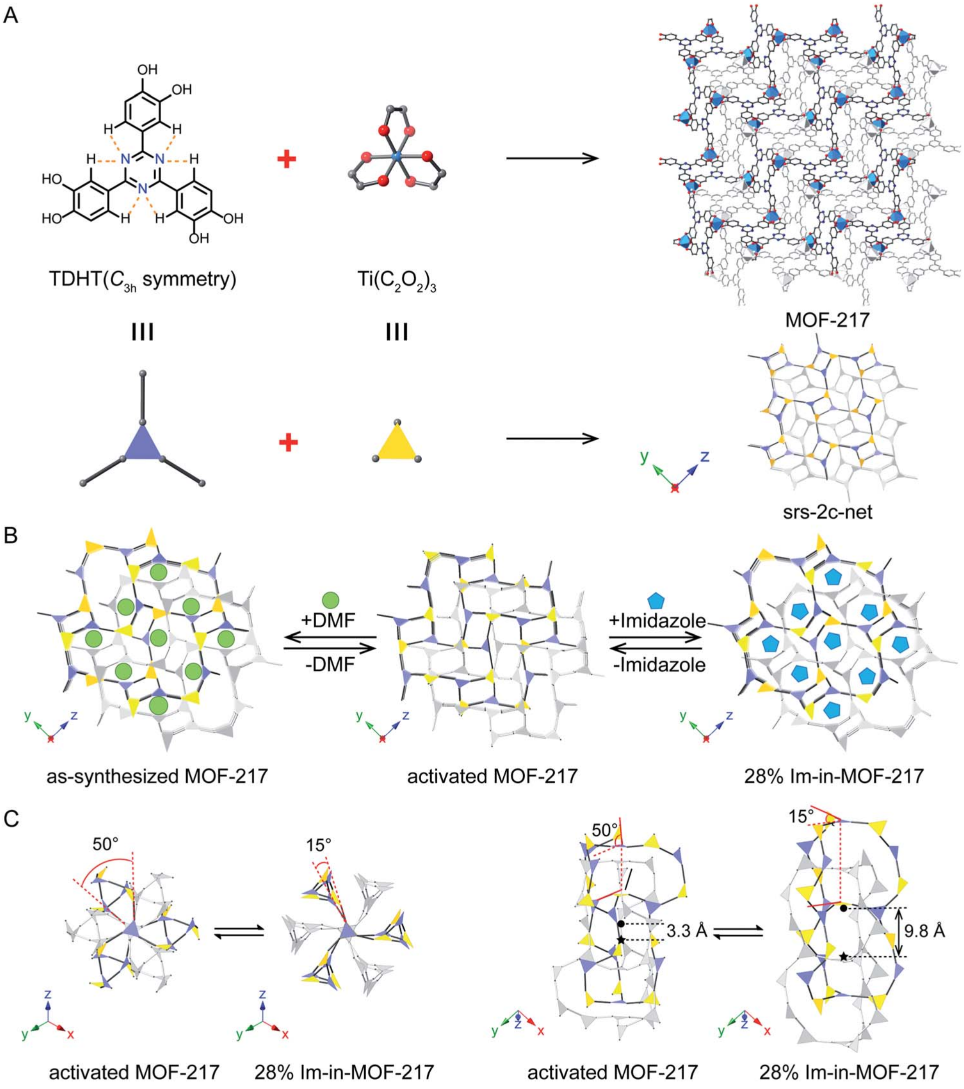

Fig. 1 (A) Structure and topology analysis of MOF-217 (purple triangle represents the TDHT linker and yellow triangle represents the TiO_6 cluster). (B) Structure transformation of MOF-217 during inclusion and removal of guest molecules (green dot represents DMF and blue pentagon represents imidazole), as shown at one direction. (C) Twist and sliding of the MOF backbone before and after including 28 wt% imidazole, where angle and distance were illustrated at two different directions, respectively.

a three-dimensional (3D) titanium catecholate framework, MOF-217, with 2-fold interpenetrated **srs** topology (Fig. 1A), where dynamics between frames was observed upon the inclusion and removal of guest molecules (Fig. 1B). This MOF was composed of a C_{3h}-symmetry catecholate linker, TDHT, capable of dihedral angle change at catecholate units (Fig. S1A†), therefore inducing both twist and shift between different sets of frames (Scheme 1 and Fig. 1C). The structure dynamics was investigated by single crystal X-ray diffraction (SXRD), where the change in both the unit cell and interframe distance was clearly observed. Powder X-ray diffraction (PXRD) data showed that the inclusion and removal of imidazole into this MOF resulted in 21% change in unit cell volume. The dihedral angle between the TDHT linker (purple triangle in Fig. 1C) and TiO_6 cluster (yellow triangle in Fig. 1C) at the opposite position of the same pore on the same frame was twisted from 15° to 50°, while the interframe distance switched between 9.8 Å and 3.3 Å. The accommodation of imidazole into pores of MOF-217 led to drastic promotion in proton conductivity by four orders of magnitude in comparison to the activated MOF. MOF-217 with 28% of imidazole by weight, 28% Im-in-MOF-217, exhibited a proton conductivity of 1.1×10^{-3} S cm^{-1} at 100 °C and can be operated for 23 hours at 85 °C, providing a new approach for the design of molecular based anhydrous proton conductors.

Results and discussion

Titanium MOFs are known to exhibit excellent chemical stability due to the strong Ti–O bond in their structures.[25] Unlike the large family of stable MOFs constructed using Zr clusters,[26,27] MOFs composed of Ti clusters are relatively rare.[28–34] This is mainly attributed to the fast hydrolysis of titanium precursors in the reaction, disfavouring the crystallization process. Here, the synthesis of MOF-217 was conducted by solvothermal reaction of 2,4,6-tri(3,4-dihydroxyphenyl)-1,3,5-triazine (TDHT) with titanium isopropoxide (TTIP) in a Schlenk tube. Precise control of the reaction temperature and moisture level was implemented to reach a balance between hydrolysis of Ti precursors and deprotonation of catechol linkers. If the reaction temperature dropped below 150 °C, insufficient dimethylammonium cations (DMA ions) could be generated for the removal of protons from catechol linkers, resulting in the formation of undesirable amorphous products. Therefore, MOF-217 was grown at 180 °C for 48 hours to yield red octahedral shaped crystals with suitable size for SXRD analysis. It was worth noting that the use of anhydrous *N*,*N*-dimethylformamide (DMF) didn't improve the crystallinity of MOFs. In contrast, regular analytical pure DMF with a trace amount of water was suited to give large single crystals.

The phase purity of MOF-217 was confirmed by the singular nature of the octahedral crystal morphology as shown in the optical microscopy image and the crystallinity of MOF-217 was evidenced by its sharp peaks in the PXRD pattern (Fig. S6†). The atomic structure of MOF-217 was identified by SXRD performed on its single crystal at 100 K, revealing a space group of $Pa\bar{3}$ (Table S1†). SXRD data were also collected at elevated temperature, 200 K and 250 K (Tables S2 and S3†), where the $Pa\bar{3}$ space group remained unchanged. In the crystal structure of MOF-217, each Ti ion was coordinated with six oxygen atoms from three TDHT linkers to give a distorted octahedral shape (Fig. S8†). The linkage of a three-connecting TiO_6 cluster and tritopic catecholate linker resulted in a typical [3 + 3] **srs** topology with a 2-fold interpenetrated structure (Fig. 1A).[35]

The design and synthesis of TDHT linkers is the key to give twist and sliding dynamics in MOF-217. MOFs based on catecholate linkers have been successfully synthesized, including Ti-MOF.[28,36,37] Most of the catecholate linkers in previous studies are composed of fused rings and usually have high symmetry with a rotational operation axis or mirror planes in between the adjacent –OH groups in the same catechol ring (Fig. S1B†). TDHT linkers in this work exhibited C–C single bonds between the centre triazine ring and the catechol ring, with one –OH group at both *meta*- and *para*- positions. This allowed for the possibility of rotation along the C–C bond, where the TiO_6 clusters are not on the rotation operation axis along the C–C bond. Unlike rigid catechol linkers in previous work, the rotation along the C–C bond in TDHT led to the change of C_{3h} symmetry of the TDHT linker to C_3 symmetry, thus inducing dynamics into the backbone of MOF-217 (Fig. S1A† and 1B). This symmetry change involved the breaking of hydrogen bonds between nitrogen atoms in triazine rings and hydrogen atoms in adjacent catechol rings. The structure dynamics was clearly observed in SXRD studies, where the unit cell parameters of the same crystal changed as the temperature increased, $a = 20.9953(3)$ Å at 100 K, and $a = 21.1222(4)$ Å at 250 K. The change in the bond length of C5–C7 is more obvious, 1.481(3) Å at 100 K, and 1.470(2) Å at 250 K (Table S4†). In addition, the distance between two interpenetrated frames in single crystal data was increased from 6.8 Å at 100 K to 7.0 Å at 250 K, indicating the expansion of the net and the shift between frames (Fig. S9 and Table S5†).

The formation of the Ti–O bond was confirmed by the presence of a characteristic Ti–O stretching peak,[38] 633 cm^{-1}, in the Fourier transfer infrared spectrum (FTIR) of the activated MOF-217 (Fig. S10†). The complete deprotonation of the TDHT linker was evidenced by the disappearance of O–H stretching peaks in MOF-217 (Fig. S11†), as all of the –OH groups in the TDHT linker were coordinated with Ti cations. X-ray photoelectron spectroscopy (XPS) analysis of the activated sample revealed the coexistence of Ti^{3+} and Ti^{4+} in the MOF backbone, where two peaks were unambiguously observed in the Ti 2p profile (Fig. S13†). This was consistent with the presence of the Ti^{3+} signal, $g = 1.924$, in the electron paramagnetic resonance (EPR) spectrum of the same sample (Fig. S14†). Surprisingly, an additional EPR signal with a g value of 2.005 was observed, which can be assigned to semiquinone radicals.[39] It was known that catechol can be partially charged to form semiquinone, which explained the presence of Ti^{3+} in the MOF structure.[40] This was also reflected in the irregular bond lengths of C–O and C–C adjacent to Ti1 in the single crystal structure of MOF-217 at different temperatures (Table S4†), a phenomenon also observed in previous report of a cobalt-based catecholate MOF.[40] MOF-217 exhibited thermal stability up to 300 °C in air as revealed by thermogravimetric analysis (TGA) (Fig. S15†). Proton nuclear magnetic resonance (^{1}H-NMR) study of the digested MOF sample in DCl/DMSO-d_6 solution determined the presence of compensatory negative charges, DMA cations, in the framework (Fig. S16†). Quantified analysis showed that the ratio of DMA cations to TDHT linkers is 1.58 : 1. This combined with the elemental analysis (EA) (Table S6†), giving a formula of $[Ti(TDHT)(Me_2NH_2)_{1.58}(DMF)_{0.15}(MeOH)_{0.5}(NBu_4Br)_{0.15}(H_2O)_{2.25}]$ for MOF-217. PXRD was also performed on MOF-217 crystals after immersion in water, a HCl aqueous solution with pH = 4 or a NaOH aqueous solution with pH = 11 for 50 hours, where the PXRD patterns were essentially the same as those of the original MOF, indicating the high chemical stability of MOF-217 (Fig. S17†).

The structure dynamics of MOF-217 is favourable to its proton conductivity. MOFs have been successfully applied as efficient proton conductors, taking advantage of the inclusion of small molecules into porous crystals.[41–46] Different from MOF-based proton conductors capable of backbone distortion (Scheme 1A),[14–17] MOF-217 in this study exhibited a different type of structure dynamics, twist and sliding between the interpenetrated frames (Scheme 1D). We found that this new type of dynamics offered excellent accommodation of molecules, here imidazole, a proton carrier known to promote the proton conductivity of solid-state porous materials when introduced into their pores.[47–50] The inclusion of imidazole into MOF-217 led to drastic boost in proton conductivity, from 1.9×10^{-7} S cm^{-1} to 1.1×10^{-3} S cm^{-1} at 100 °C. Prior to the detailed discussion on their proton conductivities, we studied the structure dynamics induced by the pore filling of imidazole molecules. The imidazole content in MOF-217 can be precisely tuned from 16% to 32% by weight (1.8 imidazole for 1 Ti cations to 4.5 imidazole for 1 Ti cations), where the accurate imidazole content in each sample was simultaneously quantified by TGA and EA (Fig. S18 and Table S8†). PXRD studies were performed on MOF-217 with different imidazole contents, using the activated MOF sample as the control (Fig. S20†). MOF-217 filled with 16% of imidazole by weight exhibited a PXRD pattern similar to that of the activated MOF. As the imidazole content increased to 18% by weight, however, systematic variation in both peak positions and intensities were observed, indicating the change of unit cell parameters as a result of structure dynamics of MOF-217. These systematic changes continued to take place until the imidazole content increased to 28% by weight (3.6 imidazole for 1 Ti cations), where the pores were saturated. Further increase of the imidazole content resulted in the deposition of imidazole crystals outside MOF pores (Fig. S21†), which can be reflected in the presence of extra peaks in PXRD patterns (Fig. S20†). In order to unveil the quantitative change in unit cell parameters, Pawley refinements were performed on small-angle X-ray scattering (SAXS) data of these

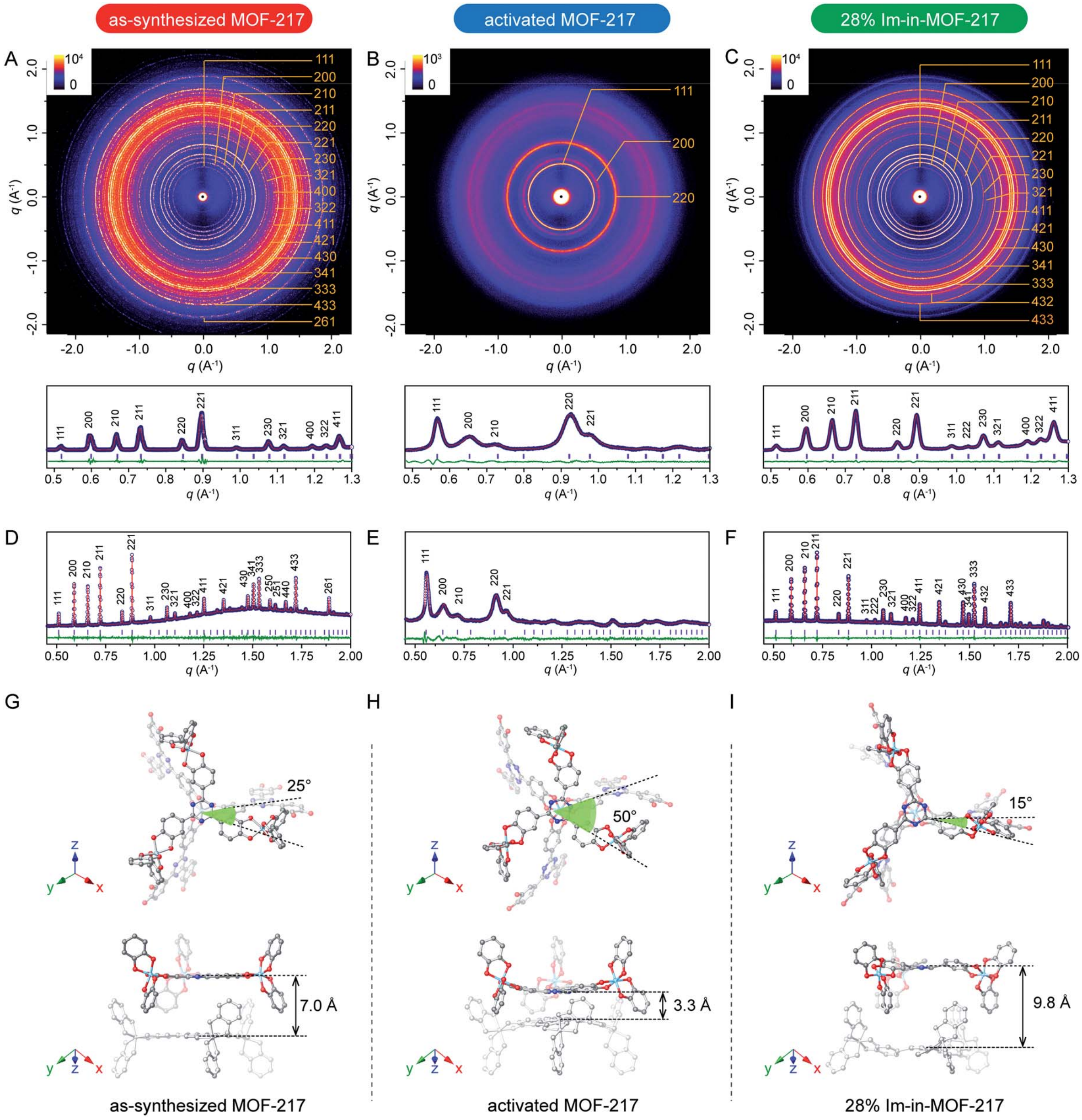

Fig. 2 Information on the structure dynamics of MOF-217 samples upon removing solvent molecules and introducing imidazole molecules. (A), (B), and (C) 2D SAXS images ($\lambda = 1.540\,56$ Å) and Pawley refinement of experimental SAXS data for the as-synthesized MOF-217, activated MOF-217 and 28% Im-in-MOF-217, respectively, where blue circles represent experimental data; red lines represent calculated data; green lines show the difference and purple bars show the Bragg position. (D), (E), and (F) Pawley refinement of experimental synchrotron data ($\lambda = 0.6526\,32$ Å) for the as-synthesized MOF-217, activated MOF-217 and 28% Im-in-MOF-217, respectively, where blue circles represent experimental data; red lines represent calculated data; green lines show the difference and purple bars show the Bragg position. (G) the single crystal structure of MOF-217 at 250 K and (H) simulated structure of MOF-217-activated. (I) the refined structure of 28% Im-in-MOF-217 determined by Rietveld refinement based on synchrotron data ($\lambda = 0.8857\,14$ Å, Fig. S21†). These defined crystal structures based on X-ray diffraction data were displayed at the same direction to show the twist and sliding dynamics.

samples (Fig. 2A to C), where low convergence residuals were achieved in these refinements for all these samples. 21% change in unit cell volume was observed between the activated sample and 28% Im-in-MOF-217 (Table S9†). PXRD data were also collected using a synchrotron X-ray source (Fig. 2D to F and S22†), which allowed for Rietveld refinement. The refinement result gave a satisfactory residual, revealing the twist within the same frame along the [111] axis and the sliding between different frames upon the filling of imidazole into pores (Fig. 2G to I). Specifically, the angle between opposite triangular counterparts (purple and yellow triangles in Fig. 1C), representing the tri-topic linker and TiO_6 cluster, switched from 15° to 50°, while the interframe distance tuned from 9.8 Å to 3.3 Å. This clearly demonstrated the capability of drastic structure dynamics in this double interpenetrated MOF.

Variable temperature *in situ* PXRD (VT-PXRD) was performed on the as-synthesized MOF-217 with the temperature range from 25 °C to 100 °C, as shown in Fig. S24.† Systematic changes in both peak positions and intensities were observed, indicating dynamics of the structure upon temperature variation. After the VT-PXRD test, this sample was solvated by immersion in DMF. The sharp peaks in the PXRD pattern and the excellent match to that of the as-synthesized sample further confirmed the thermal stability of MOF-217. In addition, immersion of activated MOF-217 back into the solvents led to the regeneration of its crystallinity (Fig. S25†). Also, we synthesized a previously reported Ti-MOF, Ti-CAT-5, with similar topology but a different symmetry in the organic linker (Fig. S1B†). Imidazole filling into its pores in an amount similar to that in MOF-217 was performed (Fig. S19 and Table S8†). However, neither the peak position nor the peak intensity was varied upon the inclusion of imidazole in Ti-CAT-5 (Fig. S23†), which is distinctively different from that observed in MOF-217. This again illustrated the importance of structure dynamics for the appropriate accommodation of imidazole molecules.

The proton conductivities of activated MOF-217 and the ones with imidazole filling in pores were tested by alternating current (ac) impedance spectroscopy, using Ti-CAT-5 counterparts as the control. Nyquist plots from the impedance test of these samples were collected at elevated temperature (30–100 °C) under a nitrogen atmosphere. Based on the impedance experiment, the proton conductivity of activated MOF-217 was calculated, *e.g.* 1.9×10^{-7} S cm^{-1} at 100 °C, which was similar to that of Ti-CAT-5, 3.8×10^{-8} S cm^{-1} at the same temperature (Fig. S30 and S31†). Analysis of the impedance at various temperatures revealed the Arrhenius plot of each sample that gave their corresponding activation energies. Based on the activation energy, there are two different mechanisms for proton conduction in general: (1) vehicle mechanism, transferring protons by the diffusion of protonated carriers with activation energy more than 0.4 eV, and (2) Grotthuss mechanism, transferring protons between the H-donor and acceptor with activation energy less than 0.4 eV.[51] Activation energies derived from these slopes in Arrhenius plots (Fig. 3B) were 0.89 eV for MOF-217 and 0.24 eV for Ti-CAT-5, respectively, both in activated form. In this regard, the proton conduction for MOF-217 is the vehicle mechanism, distinctively different from that of Ti-CAT-5. Moreover, protons on DMA cations are hopping along with the hydrogen bond network in Ti-CAT-5, while DMA cations are diffusing through the framework of MOF-217 for proton conduction. High temperature may destroy the hydrogen bond network in Ti-CAT-5, thus resulting in the decrease in the mobility of protons and proton conductivity. In contrast, higher temperature will favour the structure dynamics of MOF-217, which provides a higher degree of freedom for the transfer of DMA cations, therefore increasing the mobility of proton carriers.

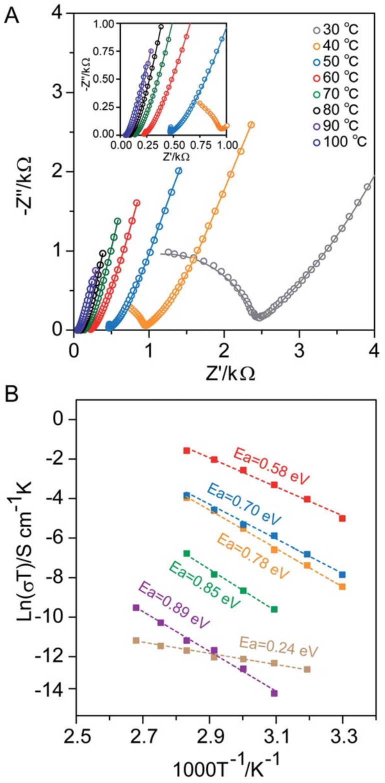

Fig. 3 (A) Nyquist plots for 28% Im-in-MOF-217 at different temperatures. (B) Arrhenius plots for 28% Im-in-MOF-217 (red), 28% Im-in-Ti-CAT-5 (blue), 23% Im-in-MOF-217 (orange), 16% Im-in-MOF-217 (green), activated MOF-217 (purple), and activated Ti-CAT-5 (khaki). Circles represent values from experiments, while dashed lines show their fitting slopes. For imidazole filled materials, their activation energies were calculated based on proton conductivities below 80 °C.

MOF-217 with 16% to 28% of imidazole by weight into the pores exhibited dramatically improved proton conductivity, 1.3 $\times 10^{-5}$ and 1.1×10^{-3} S cm^{-1} at 100 °C (Fig. S32, S33† and 3A). The activation energies of these samples were also derived using the data up to 80 °C (Fig. 3B), at which stable operation was achieved. As the imidazole content increased, the activation energy decreased gradually. Molecular dynamic calculations were carried out to assess the radial distribution functions (RDFs) for the distance between H-acceptors and H-donors (Fig. S37 to S39†), and the number of H-bonds in MOF-217 (Fig. S40†) with different imidazole contents. The results revealed the formation of a larger portion of H-bonds between the N atom in the imidazole and the O atom in the MOF structure, as imidazole was introduced. Therefore, a mixed mechanism of both vehicle and Grotthuss was likely to be present, which is consistent with the decreased activation energies. The increase in the imidazole content in MOF pores led to a more pronounced contribution from the interaction between the proton carrier and MOF, hence the further promotion in proton conductivity.

The proton conductivity of a material is dictated by both the concentration and mobility of proton carriers within this material.[47] Comparing between MOF-217 and Ti-CAT-5 with an identical imidazole content (28% by weight), drastically higher proton conductivity was observed in MOF-217, 1.1×10^{-3} S cm^{-1} at 100 °C (Fig. 3A and S34†). This value is four orders of magnitude higher than that of activated MOF-217, one magnitude higher than that of 28% Im-in-Ti-CAT-5 under identical conditions, and is among the best performing MOF materials under similar conditions (Tables S10 and S11†). The activation energy of 28% Im-in-MOF-217 was lower than that of 28% Im-in-Ti-CAT-5 (Fig. 3B), indicating more involvement of MOF frames in proton conduction. This is likely due to the better contact between the MOF and imidazole in the pores, another advantage of flexibility between interpenetrated sets. The recycle test was performed on 28% Im-in-MOF-217 to evaluate the dynamics and stability of the material. Continuous tests at 85 °C revealed negligible decrease in proton conductivity within 23 hours (Fig. S35†). It was worth noting that the crystallinity of MOF-217 was fully preserved throughout the entire impedance test, as evidenced by its unaltered PXRD pattern (Fig. S36†).

Conclusions

We synthesized a Ti-MOF, MOF-217, using a catecholate linker capable of switching between C_{3h} and C_3 symmetry. This MOF exhibited a double interpenetrated structure, where twist and sliding dynamics was observed upon temperature change and the inclusion of molecules into its pores. Structure dynamics in imidazole within MOF-217 offered extra freedom for proton carriers, leading to drastic promotion in its proton conductivity by four orders of magnitude. This twist and sliding dynamics introduced into MOFs represents a new way for the design of molecular based anhydrous proton conductors.

Experimental

Materials and methods

N,*N*-Dimethylformamide (DMF), methanol, petroleum ether (PE), dichloromethane (CH_2Cl_2), chloroform ($CHCl_3$), acetonitrile (MeCN), ammonium hydroxide, trifluoromethanesulfonic acid (CF_3SO_3H), imidazole, and sodium sulfate (Na_2SO_4) were obtained from China National Medicines Corporation Ltd. *N*,*N*-Dimethylformamide (DMF, anhydrous, 98%) and methanol (anhydrous, 98%) were purchased from J&K Chemical Co. Boron tribromide (BBr_3, 1.0 M in CH_2Cl_2) was purchased from Aladdin. Titanium(IV) isopropoxide (TTIP), tetrabutylammonium bromide (NBu_4Br), amylamine and 3,4-dimethoxybenzonitrile were purchased from Sigma Aldrich Chemical Company. 2,3,6,7,10,11-Hexahydroxytriphenylene (HHTP) was obtained from TCI. Chloroform and dichloromethane were dried using freshly activated molecular sieves 4Å prior to use. Other chemicals were used without further purifications. All manipulations of air and moisture sensitive materials were conducted under a nitrogen atmosphere in a glovebox or on a Schlenk line.

Synthesis and activation of MOF-217

TDHT (12 mg, 0.030 mmol) was dissolved in 400 μl DMF and frozen with a bath of liquid nitrogen in a Schlenk tube. NBu_4Br (10 mg, 0.031 mmol) was dissolved in 400 μl DMF and then 100 μl methanol with 4 μl amylamine as the modulator was added. The solution of titanium isopropoxide [Ti(i-OPr)$_4$, 7.5 μl, 0.025 mmol] in 200 μl DMF was injected quickly into this frozen system. These reactants were immediately sealed and vacuumed through a freeze–pump way. Reaction was naturally turned to ambient temperature, stirring for 30 minutes and heating at 180 °C for 48 hours, and then red octahedral shaped crystals were obtained. The as-synthesized sample was refluxed using DMF for 1 day and methanol for another 1 day. Next, the MOF sample was transferred to a supercritical CO_2 drier and washed 5 times with liquid CO_2 (liquid CO_2 was refreshed every 15 minutes) for removing residual solvents. During this process, the chamber was heated up to 38 °C and held on the supercritical condition (typically 1300 psi) for 45 minutes, and then CO_2 was slowly bled from the chamber for nearly 6 hours. Finally, activated MOF-217 was obtained.

Synthesis and activation of Ti-CAT-5

Ti-CAT-5 was synthesized by an improved procedure based on reference.[28] Titanium isopropoxide [Ti(i-OPr)$_4$, 9 μl, 0.03 mmol], HHTP (10 mg, 0.030 mmol), and NBu_4Br (10 mg, 0.031 mmol) were dissolved in 1 ml anhydrous DMF and 30 μl anhydrous methanol, with 4 μl amylamine as the modulator. Then the mixture was transferred into an 8 mm dia glass tube which was quickly frozen and vacuumed through a freeze–pump way. The tube was put into an oven and stood for 48 hours at 180 °C. After the reaction was cooled down to room temperature, brown powder was collected by centrifugation at 11 000 rpm for 5 minutes. The as-synthesized sample was washed using DMF 5 times and MeCN 9 times, and then dried under vacuum at room temperature for 24 hours to get the activated sample. Characterization experiments such as PXRD, IR, XPS, TGA, EA and N_2 absorption were performed to identify the successful synthesis of Ti-CAT-5 (Fig. S7, S12, S13, S15, S26–S28 and Table S8†).

Imidazole loading and ac impedance experiment

Imidazole was ground with activated MOF-217 and sealed in a tube, and then stood at 120 °C under reduced pressure overnight. Also, imidazole was embedded into Ti-CAT-5 in the same way as proton conduction comparison. Powdery samples were pressed into a pellet with 12 mm dia and ~0.4 mm thickness. Each pellet was sandwiched using two stainless electrodes and a spring for good contact, and sealed into a button cell. Considering the humidity in air, this process was manipulated in a N_2 glovebox. Both sides of the cell were attached with silver wires, and then put into a homemade chamber for temperature control. Alternating current (ac) impedance analysis was performed on a Biologic VPM-3 electrochemical workstation in the 1 Hz to 10 MHz frequency range and with 10 mV input voltage amplitude at different temperatures (30–100 °C). Zsimpwin software was used to simulate an equivalent circuit (Fig. S29†) to match the Nyquist plots and obtain resistance values. Finally, resistance values were input in the equation ($\sigma = L/RS$) to get conductivity values.

Conflicts of interest

There are no conflicts to declare.

Acknowledgements

We thank the support from beamline BL15XU in Japan Synchrotron Radiation Research Institute (SPring-8), BL14B1, BL17U and BL18U1 in Shanghai Synchrotron Radiation Facility (SSRF), and Core Research Facilities of Wuhan University. We thank Prof. Xingmin Zhang, Prof. Wen Wen, and Dr. Zier Yan for their help with synchrotron data and Prof. Guangfeng Wei and Prof. Shule Liu for the discussion on computational work. We also thank Prof. Fusheng Ke, Prof. Dong Gu, Jin Liu, Gaoli Hu, Zhenjin Liang, Chao Wang, Haoyu Liu, Yi Zhou, Xiaohui Xu, Xudong He, Haoqing Jiang, Gongwei Wang, and other members from Wuhan University for their valuable discussion and generous help. This project was supported by the National Natural Science Foundation of China (21471118, 21971199, 91545205, and 91622103), National Key Research and Development Project of China (2018YFA0704000), and Fundamental Research Funds for the Central Universities (2042019kf0205).

Notes and references

1 K. Henzler-Wildman and D. Kern, *Nature*, 2007, **450**, 964–972.
2 J. D. Kahn, E. Yun and D. M. Crothers, *Nature*, 1994, **68**, 163–166.
3 R. G. Smock and L. M. Gierasch, *Science*, 2009, **324**, 198–203.
4 D. Holden, S. Y. Chong, L. Chen, K. E. Jelfs, T. Hasell and A. I. Cooper, *Chem. Sci.*, 2016, **7**, 4875–4879.
5 C. Gu, N. Hosono, J.-J. Zheng, Y. Sato, S. Kusaka, S. Sakaki and S. Kitagawa, *Science*, 2019, **363**, 387–391.
6 S. Horike, S. Shimomura and S. Kitagawa, *Nat. Chem.*, 2009, **1**, 695–704.
7 H. Yang, F. Guo, P. Lama, W.-Y. Gao, H. Wu, L. J. Barbour, W. Zhou, J. Zhang, B. Aguila and S. Ma, *ACS Cent. Sci.*, 2018, **4**, 1194–1200.
8 Y.-X. Ma, Z.-J. Li, L. Wei, S.-Y. Ding, Y.-B. Zhang and W. Wang, *J. Am. Chem. Soc.*, 2017, **139**, 4995–4998.
9 T. Sun, L. Wei, Y. Chen, Y. Ma and Y.-B. Zhang, *J. Am. Chem. Soc.*, 2019, **141**, 10962–10966.
10 Z. Wang, N. Sikdar, S.-Q. Wang, X. Li, M. Yu, X.-H. Bu, Z. Chang, X. Zou, Y. Chen, P. Cheng, K. Yu, M. J. Zaworotko and Z. Zhang, *J. Am. Chem. Soc.*, 2019, **141**, 9408–9414.
11 H. Furukawa, J. Kim, N. W. Ockwig, M. O'Keeffe and O. M. Yaghi, *J. Am. Chem. Soc.*, 2008, **130**, 11650–11661.
12 H. Deng, S. Grunder, K. E. Cordova, C. Valente, H. Furukawa, M. Hmadeh, F. Gándara, A. C. Whalley, Z. Liu, S. Asahina, H. Kazumori, M. O'Keeffe, O. Terasaki, J. F. Staddart and O. M. Yaghi, *Science*, 2012, **336**, 1018–1023.
13 H. C. Zhou and S. Kitagawa, *Chem. Soc. Rev.*, 2014, **43**, 5415–5418.
14 E. Eisbein, J.-O. Joswig and G. Seifert, *J. Phys. Chem. C*, 2014, **118**, 13035–13041.
15 Y. Ye, X. Wu, Z. Yao, L. Wu, Z. Cai, L. Wang, X. Ma, Q.-H. Chen, Z. Zhang and S. Xiang, *J. Mater. Chem. A*, 2016, **4**, 4062–4070.
16 D. A. Levenson, J. Zhang, P. M. Szell, D. L. Bryce, B. S. Gelfand, R. P. Huynh, N. Fylstra and G. K. H. Shimizu, *Chem. Mater.*, 2020, **32**, 679–687.
17 F. Yang, G. Xu, Y. Dou, B. Wang, H. Zhang, H. Wu, W. Zhou, J. R. Li and B. Chen, *Nat. Energy*, 2017, **2**, 877–883.
18 H. Deng, M. A. Olson, J. F. Stoddart and O. M. Yaghi, *Nat. Chem.*, 2010, **2**, 439–443.
19 W. Liang, P. M. Bhatt, A. Shkurenko, K. Adil, G. Mouchaham, H. Aggarwal, A. Mallick, A. Jamal, Y. Belmabkhout and M. Eddaoudi, *Chem*, 2019, **5**, 950–963.
20 S. B. Choi, H. Furukawa, H. J. Nam, D. Y. Jung, Y. H. Jhon, A. Walton, D. Book, M. O'Keeffe, O. M. Yaghi and J. Kim, *Angew. Chem., Int. Ed.*, 2012, **51**, 8791–8795.
21 T. K. Maji, R. Matsuda and S. Kitagawa, *Nat. Mater.*, 2007, **6**, 142–148.
22 H. Sato, W. Kosaka, R. Matsuda, A. Hori, Y. Hijikata, R. V. Belosludov, S. Sakaki, M. Takata and S. Kitagawa, *Science*, 2014, **343**, 167–170.
23 C. Serre, F. Millange, C. Thouvenot, M. Noguès, G. Marsolier, D. Louër and G. Férey, *J. Am. Chem. Soc.*, 2002, **124**, 13519–13526.
24 A.-X. Zhu, Q.-Y. Yang, A. Kumar, C. Crowley, S. Mukherjee, K.-J. Chen, S.-Q. Wang, D. O' Nolan, M. Shivanna and M. J. Zaworotko, *J. Am. Chem. Soc.*, 2018, **140**, 15572–15576.
25 N. Steunou, G. Maurin, T. Uemura and C. Serre, *Nat. Commun.*, 2018, **9**, 1660.
26 A. J. Howarth, Y. Liu, P. Li, Z. Li, T. C. Wang, J. T. Hupp and O. K. Farha, *Nat. Rev. Mater.*, 2016, **1**, 15018.
27 Y. Bai, Y. Dou, L.-H. Xie, W. Rutledge, J.-R. Li and H. C. Zhou, *Chem. Soc. Rev.*, 2016, **45**, 2327–2367.
28 N. T. Nguyen, H. Furukawa, F. Gándara, C. A. Trickett, H. M. Jeong, K. E. Cordova and O. M. Yaghi, *J. Am. Chem. Soc.*, 2015, **137**, 15394–15397.
29 M. Dan-Hardi, C. Serre, T. Frot, L. Rozes, G. Maurin, C. Sanchez and G. Férey, *J. Am. Chem. Soc.*, 2009, **131**, 10857–10859.
30 C. Li, H. Xu, J. Gao, W. Du, L. Shangguan, X. Zhang, R.-B. Lin, H. Wu, W. Zhou, X. Liu, J. Yao and B. Chen, *J. Mater. Chem. A*, 2019, **7**, 11928–11933.
31 S. Yuan, T. F. Liu, D. Feng, J. Tian, K. Wang, J. Qin, Q. Zhang, Y.-P. Chen, M. Bosch, L. Zou, S. J. Teat, S. J. Dalgarno and H. C. Zhou, *Chem. Sci.*, 2015, **6**, 3926–3930.
32 B. Bueken, F. Vermoortele, D. E. P. Vanpoucke, H. Reinsch, C.-C. Tsou, P. Valvekens, T. De Baerdemaeker, R. Ameloot,

C. E. A. Kirschhock, V. Van Speybroeck, J. M. Mayer and D. De Vos, *Angew. Chem., Int. Ed.*, 2015, **54**, 13912–13917.

33 W.-H. Fang, L. Zhang and J. Zhang, *Chem. Soc. Rev.*, 2018, **47**, 404–421.

34 M. W. Logan, J. D. Adamson, D. Le and F. J. Uribe-Romo, *J. Mater. Chem. A*, 2017, **5**, 11854–11863.

35 S. T. Hyde, M. O'Keeffe and D. M. Proserpio, *Angew. Chem., Int. Ed.*, 2008, **47**, 7996–8000.

36 M. Hmadeh, Z. Lu, F. Gándara, H. Furukawa, S. Wan, V. Augustyn, R. Chang, L. Liao, F. Zhou, E. Perre, V. Ozolins, K. Suenaga, X. Duan, B. Dunn, Y. Yamamto, O. Terasaki and O. M. Yaghi, *Chem. Mater.*, 2012, **24**, 3511–3513.

37 R. Matheu, E. Gutierrez-Puebla, M. Ángeles Monge, C. S. Diercks, J. Kang, M. S. Prévot, X. Pei, N. Hanikel, B. Zhang, P. Yang and O. M. Yaghi, *J. Am. Chem. Soc.*, 2019, **141**, 17081–17085.

38 D. Wang, R. Yu, N. Kumada and N. Kinomura, *Chem. Mater.*, 1999, **11**, 2008–2012.

39 S. Wang, T. Kitao, N. Guillou, M. Wahiduzzaman, C. Martineau-Corcos, F. Nouar, A. Tissot, L. Binet, N. Ramsahye, S. Devautour-Vinot, S. Kitagawa, S. Seki, Y. Tsutsui, V. Briois, X. Zhang, N. A. Vermeulen, Z. Huang, Y. Cui, J. Liu, M. D. Krzyaniak, Z. Li, H. Noh, M. R. Wasielewski, M. Delferro and O. K. Farha, *ACS Appl. Mater. Interfaces*, 2017, **10**, 635–641.

40 B. Li, Y. M. Zhao, A. Kirchon, J. D. Pang, X. Y. Yang, G. L. Zhuang and H. C. Zhou, *J. Am. Chem. Soc.*, 2019, **141**, 6822–6826.

41 J. A. Hurd, R. Vaidhyanathan, V. Thangadurai, C. I. Ratcliffe, I. L. Moudrakovski and G. K. H. Shimizu, *Nat. Chem.*, 2009, **1**, 705–710.

42 G. K. H. Shimizu, J. M. Taylor and S. Kim, *Science*, 2013, **341**, 354–355.

43 S. S. Park, A. J. Rieth, C. H. Hendon and M. Dincă, *J. Am. Chem. Soc.*, 2018, **140**, 2016–2019.

44 G. Xing, T. Yan, S. Das, T. Ben and S. Qiu, *Angew. Chem., Int. Ed.*, 2018, **57**, 5345–5349.

45 Y. Yang, X. He, P. Zhang, Y. H. Andaloussi, H. Zhang, Z. Jiang, Y. Chen, S. Ma, P. Cheng and Z. Zhang, *Angew. Chem., Int. Ed.*, 2020, **59**, 3678–3684.

46 S. Chandra, T. Kundu, S. Kandambeth, R. BabaRao, Y. Marathe, S. M. Kunjir and R. Banerjee, *J. Am. Chem. Soc.*, 2014, **136**, 6570–6573.

47 S. Bureekaew, S. Horike, M. Higuchi, M. Mizuno, T. Kawamura, D. Tanaka, N. Yanai and S. Kitagawa, *Nat. Mater.*, 2009, **8**, 232–237.

48 Y. Ye, W. Guo, L. Wang, Z. Li, Z. Song, J. Chen, Z. Zhang, S. Xiang and B. Chen, *J. Am. Chem. Soc.*, 2017, **139**, 15604–15607.

49 F.-M. Zhang, L.-Z. Dong, J.-S. Qin, W. Guan, J. Liu, S.-L. Li, M. Lu, Y.-Q. Lan, Z.-M. Su and H.-C. Zhou, *J. Am. Chem. Soc.*, 2017, **139**, 618–6189.

50 S. Liu, Z. Yue and Y. Liu, *Dalton Trans.*, 2015, **44**, 12976–12980.

51 P. Ramaswamy, N. E. Wong and G. K. H. Shimizu, *Chem. Soc. Rev.*, 2014, **43**, 5913–5932.